Temporal Decorrelation of GPS Satellite Signals due to Multiple Scattering from Ionospheric Irregularities

Charles S. Carrano, *Institute for Scientific Research, Boston College, Chestnut Hill, MA*
Keith M. Groves, *Air Force Research Laboratory, Hanscom AFB, MA*

BIOGRAPHY

Charles S. Carrano is a senior research physicist at Boston College's Institute for Scientific Research. He received a B.S. in mechanical engineering from Cornell University and M.S. and Ph.D. degrees in aerospace engineering from The Pennsylvania State University. His research interests include ionospheric impacts on radar, satellite communications, and the Global Positioning System.

Dr. Groves is currently a Program Manager in the Space Vehicles Directorate of the Air Force Research Laboratory where he investigates ionospheric scintillation and its impact on satellite based communication and navigation systems. He has a Ph.D. in Space Physics from MIT and a B.S. in Physics from Andrews University.

ABSTRACT

Rapid fluctuations in the amplitude and phase of the GPS satellite signals caused by scattering from ionospheric irregularities can degrade GPS performance in a number of ways. These signal fluctuations are referred to as scintillations. Severe scintillations may result in loss of lock, and even when lock is maintained, they may cause errors decoding the GPS data messages and corrupt estimation of the ranges to the GPS satellites. Several previous attempts to model the effects of ionospheric scattering on GPS performance have focused on the depth of signal fading, as quantified by the S_4 index, as the appropriate parameterization to use for the ionospheric perturbation of the signal. The S_4 index may not be the best parameter for this purpose, however, because it is limited in several respects. Firstly, the S_4 index is independent of the rate of signal fading which has a direct impact on the stress of the GPS tracking loops. Secondly, under strong scattering conditions the S_4 index saturates to a value near unity, irrespective of the strength of the ionospheric perturbation. On the other hand, the decorrelation time characterizes the rate of signal fading and continues to vary with the strength of the ionospheric perturbation once when the S_4 index has saturated.

In this paper we characterize the temporal decorrelation of the GPS satellite signals using 20 Hz observations collected at Ascension Island (7.96ºS, 14.41ºW, dip latitude 12.4ºS) on 5-19 March 2002, during solar maximum conditions. We explore the relationships between the ionospheric scintillation parameters, loss of lock, and signal reacquisition time and provide empirical fits to the probability of losing lock for use in modeling and simulation studies. Our results suggest that rate of signal fluctuation, in addition to the depth of signal fading, should be considered when modeling GPS receiver performance in the presence of scintillation. We observed that the probability of loss of lock and likelihood of extended signal reacquisition times depend on the velocity of satellite motion with respect to the magnetic field and plasma drift, which are relatively predictable *a priori* in the equatorial region.

INTRODUCTION

Air Force Research laboratory conducted a campaign to monitor GPS scintillations at Ascension Island during the solar maximum period 5-19 March 2002. One of the several GPS receivers operated during the campaign was an Ashtech Z-XII survey grade model with a choke ring antenna. This receiver reported samples of C/No and carrier phase for the L1 and L2 carrier signals at 20 Hz. Intense scintillation activity (S_4~1) was encountered on all nights except one (March 6 was quiet), and severe impacts to GPS tracking performance and positioning accuracy were observed.

The purpose of this paper is to 1) characterize the signal fluctuations observed in terms of various scintillation parameters, 2) report the occurrences of loss of lock and the satellite reacquisition time, 3) characterize the probability of loss of lock as functions of the scintillation parameters, and 4) provide empirical fits to the

23rd International Technical Meeting of the Satellite Division of
The Institute of Navigation, Portland, OR, September 21-24, 2010

probability of losing lock for use in modeling and simulation studies.

The S_4 index is the standard deviation of normalized signal intensity fluctuations and is directly related to the probability that signal fades will reach a particular level [Basu et al., 1987]. Loss of lock is more likely occur when the GPS signal level drops below the fade margin of the receiver's internal tracking loops. Therefore, it is not surprising that the S_4 index is closely related to the probability of losing lock. Figure 1 shows a scatter plot of S_4 versus time for all GPS satellites in view above 30° for all nights of the campaign. On average, the scintillation activity started approximately 1.5 hours after local sunset, and persisted for about 5-6 hours (roughly until local midnight). The data samples in the plot are colored red if a loss of lock event occurred and green otherwise. We will make our working definition of loss of lock more precise below. It is clear from the figure that the density of loss of lock events increases with increasing S_4.

Figure 2 shows the likelihood that the error in the horizontal position reported by the receiver reached a particular level. For example, the error in horizontal position error was less than the green curve 50% of the time, less than the blue curve 75% of the time, and less than the red curve 95% of the time. To generate these statistics, we took the 1 Hz samples of the position reported by the receiver and computed the horizontal deviations from the median position over the campaign. These deviations were binned into 60 second intervals and then sorted. The percentile of occurrence was obtained by sampling the sorted deviations at the desired percentile of occurrence. Brief excursions exceeding 80 meters were observed on a couple of nights, the largest and most frequent excursions occurring on 16 March (not shown). It is clear from Figures 1 and 2 that GPS position errors were largest when loss of lock occurrences were the most frequent.

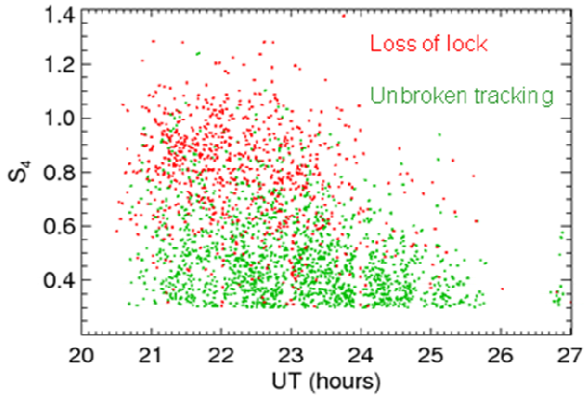

Fig. 1. Scatter plot of S_4 versus time. Local sunset at 300 km occurred at 19:10 UT. Red dots indicate loss of lock, green dots indicate unbroken (continuous) tracking.

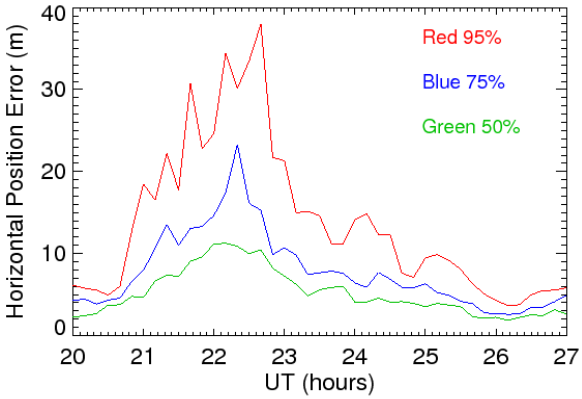

Fig. 2. The 50th, 75th, and 95th percentile horizontal error in the receiver reported position versus time.

Once the radio wave fluctuations caused by scattering from ionospheric irregularities have caused the GPS receiver to lose lock on the signal, the receiver obviously cannot continue to monitor these fluctuations until lock is restored. For the physicist, it is frustrating that the receiver cannot consistently monitor signal fluctuations during the most disturbed ionospheric conditions, which are perhaps the most interesting. For the engineer, it is frustrating that the receiver cannot monitor the RF conditions which caused its own tracking loops to fail. Instead, we must infer the cause of each loss of lock occurrence indirectly, by considering the statistics of signal fluctuations immediately preceding the loss of lock event.

Our goal is to relate the statistics of scintillation to the occurrence of loss of lock (LOL) and the time to reacquire the signal. To do this we must clearly explain how we identify loss of lock events and define the time to reacquire the signal. As an example, Figure 3 shows the L1 C/No for PRN04 during a period of intense scintillation starting at 21:07:30 UT on 12 March 2002. The red dashed line at ~420 sec shows the time of the last C/No sample prior to a gap in the data. This is a loss of lock event. As can be seen in the figure, the receiver made several failed attempts to reestablish a lock on the signal. The green dashed line at ~760 sec shows the time at which a stable lock was finally restablished, in that continuous sampling was maintained for an extended period of time. In this paper, we distinguish between the "time to next sample," which quantifies the length of the data gap, and the "reacquisition time" which quantifies the time is takes for the receiver to reestablish a stable lock of the signal. In more precise terms, we define the time to next sample as the time following a loss of lock event until the next data sample is obtained. We define the reacquisition time as the time following a loss of lock event until the first sample is obtained which is itself followed by at least 60 seconds of continuous sampling.

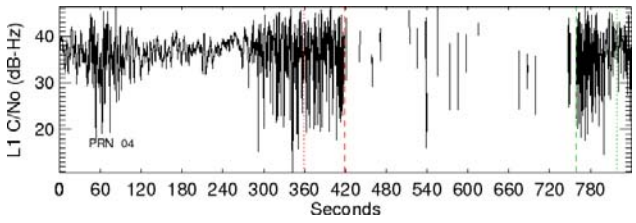

Fig. 3. Carrier to noise ratio versus time for PRN04, starting at 21:07:30 UT on 12 March 2002.

Figure 4 shows a histogram of the time to next sample for all the loss of lock events observed during the campaign. There is a strong peak in the histogram at 2.55 seconds which encompasses 95% of all the observed LOL events. This may lead one to believe that the receiver is able to recover fairly quickly after a loss of lock, but this is quite misleading as the first samples following a loss of lock are usually followed by one or more additional gaps. As discussed by Kintner et al. (2007), a GPS receiver may have difficulty reacquiring a satellite signal during scintillation, and this effect is clearly apparent in our data.

Figure 5 shows a histogram of the time it took the receiver to reacquire the signal in a stable manner after loss of lock events. On average (50% of the time) the receiver took 13.5 seconds or less to reestablish a stable lock on the signal. At the 95% percentile, it took up to 4 minutes to reestablish a stable lock on the signal. It is perhaps surprising how extended the tail of this histogram actually is. Figure 6 shows the occurrence of LOL events for which it took the receiver between 1 and 15 minutes to reestablish a stable lock on the signal. We should point out that some of the reacquisition times we observed are substantially longer than those observed in similar studies, e.g. Seo et al. [2008]. We expect that some of this discrepancy may be attributed to differences in tracking characteristics of the specific receivers considered, but since the dataset we analyzed is substantially longer (14 days versus 45 minutes in the Seo study), we may be able to better characterize the tail of the distribution.

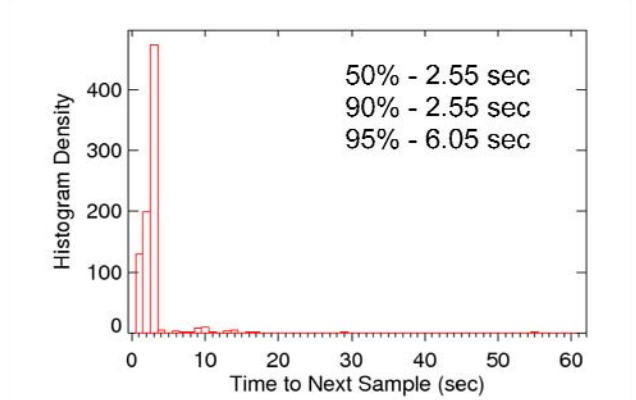

Fig. 4. Histogram of the time to next sample for all loss of lock events detected.

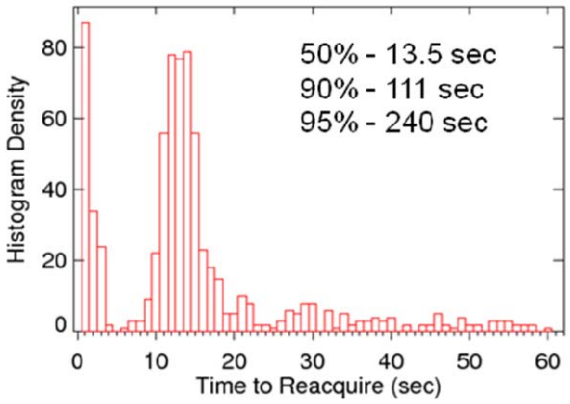

Fig. 5. Histogram of reacquisition times between 1-60 seconds for all loss of lock events detected.

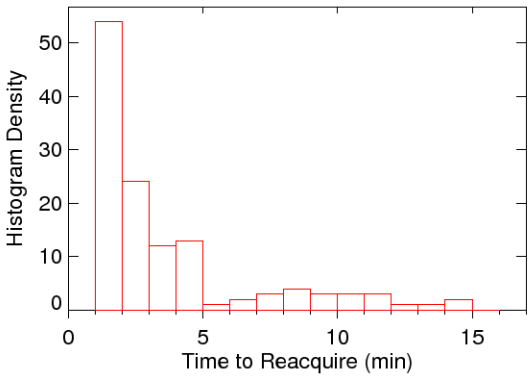

Fig. 6. Histogram of reacquisition times between 1-15 minutes for all loss of lock events detected.

DATA ANALYSIS AND METHODOLOGY

The Ashtech Z-XII receiver records the C/No and carrier phase of the GPS L1 and L2 signals at a rate of 20 Hz, and stores the data in proprietary FST/DEL binary data records. The specific technique used by the receiver to measure the C/No is unknown. In this work we subtract 40 dB from the receiver reported values to produce values which are relatively consistent with those reported by other receivers. While the absolute level of C/No is an important factor in determining the receiver response to scintillation, the S_4 index is independent of this absolute level and is unaffected by our choice of calibration.

The scintillation parameters that we compute directly from the GPS L1 C/No and carrier phase measurements include the scintillation index (S_4), the decorrelation time of intensity (τ_I), the phase spectral index (p), the phase scintillation index (σ_φ), and the value of the phase spectral density at 1 Hz (T).

To ensure that our scintillation statistics are reliable, we require that these statistics be computed over 60 second windows of continuous sampling without data gaps. Data gaps can introduce unwanted artifacts into power spectral density estimates and complicate detrending of the phase, which is necessary to remove the Doppler due to satellite motion. Another reason we require continuous sampling is to be sure the receiver's tracking loops are stable so that its reported measurements of signal intensity and phase are trustworthy.

We select the 60 second observation windows over which to compute the scintillation statistics as follows. First, gaps in the measurements are identified. Counting backwards from each data gap, the measurements are divided into as many 60 second intervals with continuous sampling as possible, until the preceding data gap or the start of the data for that satellite pass is encountered. Only data collected while the satellite is above 30° elevation are considered, so that the setting of the satellites behind ground-based obstructions are not considered as loss of lock events (since they are not caused by the ionosphere). The exclusion of low elevation data from our analysis is also necessary to reject multipath from ground-based objects. The 60 second scintillation statistics are classified into three different categories: 1) samples for which a loss of lock occurred at the end of the 60 second observation window, 2) samples which are 4 or more minutes away from the next loss of lock event, and 3) all other samples.

When we need to associate samples of the scintillation statistics with the occurrence or absence of loss of lock, we consider only those samples belonging to categories 1 and 2, and exclude samples belonging to category 3 as possibly ambiguous with regard to loss of lock. For example, in Figure 1 and also Figures 19-24, samples from category 1 are colored red to indicate loss of lock, whereas samples from category 2 are colored green to indicate continuous (unbroken) tracking. Samples from category 3 are excluded from these plots for clarity.

The S_4 index is computed as the standard deviation of normalized signal intensity (expressed in linear units, not dB). The decorrelation time is computed as the shortest lag for which the autocorrelation function of intensity attains a value of 1/2. To compute the phase parameters, cycle slips in the carrier phase are repaired (when possible, otherwise the data is discarded) and the result detrended using a 6^{th} order Butterworth high-pass filter applied in the frequency domain with a 3dB cutoff at f_c=0.1 Hz. The power spectral density (PSD) of the detrended phase is computed using Welch's method with 50% overlap [Welch, 1967]. A least squares fit in logarithm space over the frequency range 0.3-1.5 Hz is used to determine the phase spectral index (p). This particular frequency range was chosen to maximize the spectral range used for the fit while avoiding both the detrend filter cutoff at 0.1 Hz and also a peak in the receiver thermal noise that we observed to occur within the range 2-3 Hz. The value of the phase spectral density (PSD) at 1 Hz (T) is the obtained by evaluating the least squares fit at the frequency 1 Hz.

Rino [1979] derived the following relationship between the parameter T and the propagation geometry and strength of turbulence in a power-law environment:

$$T = r_e^2 \lambda^2 (L \sec\theta) G C_s \frac{\pi^{1/2}\Gamma(\nu)}{(2\pi)^{2\nu-1}\Gamma[\nu+1/2]} v_{eff}^{2\nu-1} \quad (1)$$

where

r_e = classical electron radius (2.818×10^{-15}m),
λ = signal wavelength (1.57542×10^9 Hz),
G = geometry enhancement factor,
C_s = strength of turbulence,
L = thickness of the scattering layer,
θ = zenith angle of propagation,
Γ = Euler's gamma function,
and v_{eff} = effective scan velocity.

The power-law index of the ionospheric spatial spectrum (ν) can be estimated from the measured phase spectral index as $\nu \approx p/2$. The geometrical enhancement factor is

$$G = \frac{ab}{\sqrt{AC - B^2/4}\cos\theta} \quad (2)$$

where a and b are irregularity axial ratios along and transverse to the magnetic field, respectively, and A, B, and C are geometrical parameters given by equation (41) in Rino et al. [1977]. In this paper we assume a=50, b=1 which is appropriate for equatorial field-aligned irregularities.

The effective scan velocity, v_{eff}, is the rate at which the signal line of sight scans across isocontours of phase correlation in the horizontal plane of the irregularity layer. It accounts for the effect of anisotropy on the conversion from spatial structure to temporal fluctuations. It assumes a specific irregularity layer height (we use 350 km) and also requires knowledge of the plasma drift velocity.

We obtain the plasma drift velocity from SCINDA, which uses VHF signals from geostationary satellites and the spaced receiver technique to measure the zonal plasma drift. For each night, we fit a line to the SCINDA zonal plasma drift using robust least squares, and use the linear fit to compute the effective velocity. For nights when no drift measurements were available, the average nightly drift over the campaign was used instead. Figure 7 shows an example of the zonal drift velocity measurements from SCINDA, and the linear fit to the data. Table 1 shows the parameters of the fit and the reduced chi value for the nights when SCINDA drift measurements were available. Note the relative consistency in the zonal drift

measurements from night to night. This implies that changes in satellite motion, rather than the plasma drift velocity, largely control the effective velocity variations we describe in this paper.

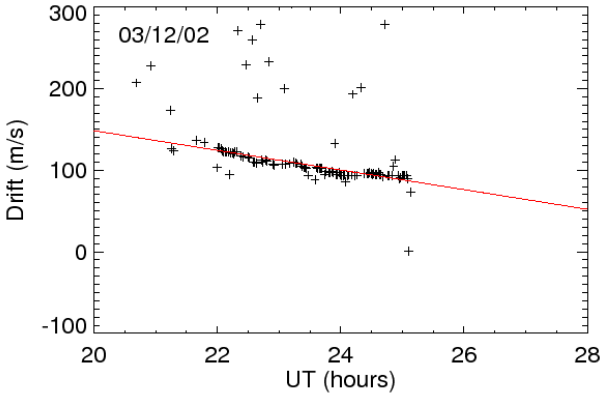

Fig. 7. Drift velocity measured by SCINDA using the spaced receiver technique on 12 Mar 2002. The red line is a robust least squares linear fit to the observations.

Table 1. Coefficients and the reduced chi value for the robust linear least squares fit of the SCINDA zonal drift velocity (v_D). The fitting function used is $v_D=c_1+c_2(t-20)$, where t is expressed in hours UT and v_D in m/s.

Day of March	c_1	c_2	χ
5	157.8	-15.3	6.2
7	169.6	-13.3	8.6
10	191.9	-18.1	5.5
11	161.2	-15.8	10.5
12	148.4	-12.0	7.5
13	165.7	-14.6	7.3
14	185.9	-18.7	11.3
15	191.0	-19.9	12.8
16	164.1	-16.2	7.7
18	186.6	-24.9	11.6
19	195.4	-23.3	9.1

The GPS satellite ephemeris is used to compute the locations of the GPS satellites. From this, the locations and velocities of the ionospheric penetration points (IPP) at 350 km are computed. The IGRF 2000 magnetic field model is then used to compute the magnetic dip and magnetic meridian angle at the penetration points. The effective scan velocity is computed from these quantities as described in Rino [1979]. We should point out that, strictly speaking, v_{eff} has no physical significance during bubble development, only during the stages of "frozen-in" plasma drift and decay. In spite of this known limitation, we use the value of v_{eff} throughout the night in order to organize the data.

Given measurements of T, we can estimate the strength of turbulence C_s from equation (1). From this we may compute the vertically integrated strength of turbulence at the 1 km scale using the identity:

$$C_k L = C_s L \left(\frac{1000}{2\pi}\right)^{2\nu+1} \qquad (3)$$

Note that the layer thickness, L, need not be known to evaluate C_kL, which is an advantage over the use of C_s in characterizing the strength of turbulence.

DECORRELATION TIME AND LOSS OF LOCK

The S_4 index quantifies the level of fluctuations in signal power at the receiver. The intensity decorrelation time τ_I quantifies the rate at which these power fluctuations are occurring. Both of these determine, on a statistical basis, whether or not the receiver's tracking loops can maintain a lock on the GPS signal.

As an example, Figures 8 and 9 show S_4, τ_I, v_{eff}, and satellite elevation versus time for PRN04 and PRN27, respectively, during a period of intense scintillation. On this evening there were 319 gaps in the raw data for PRN04 (not shown) for a total of 5873 seconds, and there were 30 gaps in the raw data for PRN27 (also not shown) for a total 199 seconds. The important question to ask is why the receiver should have dropped nearly 30 times as many data samples for PRN04 as compared to PRN27 even though the scintillation intensities (and also the satellite elevation angles) encountered along these links are similar? We suggest that the motion of the satellites with respect to the drifting plasma irregularities is responsible, which resulted in very different effective scan velocities for these two satellites. The component of the IPP velocity in the direction of the plasma drift was larger for PRN27, and as a result its effective scan velocity was smaller. The decorrelation time measured by PRN27 was correspondingly longer. The longer decorrelation time resulted in a much lower rate of loss of lock for PRN27 than for PRN04.

Each night of the campaign for which scintillation occurred exhibited similar behavior—the number of data gaps for PRN04 greatly exceeded those for PRN27. Since the GPS satellite orbits repeat with the Sidereal day, this is not surprising if the difference in tracking performance can be explained in terms of geometrical considerations rather than the details of the ionospheric scattering environment (i.e. the spatial distribution and structure of the irregularities).

We will show that under moderate to strong scintillation conditions, the decorrelation time affects both the likelihood of loss of lock and the time to reacquire the

signal. The S_4 index is still of primary importance, however, because if there were no signal fading then τ_I would have no meaning. Also, empirical evidence suggests that weak signal fades do not appear to adversely affect GPS tracking regardless of the fading rate.

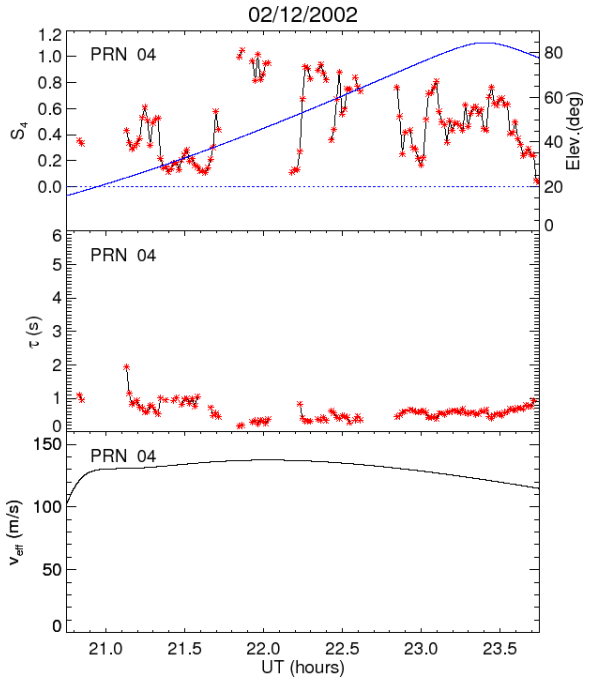

Fig. 8. Time variation of S_4 (top), τ_I (middle), and v_{eff} (bottom) for PRN04 on 12 Mar 2002. The satellite elevation is shown in blue.

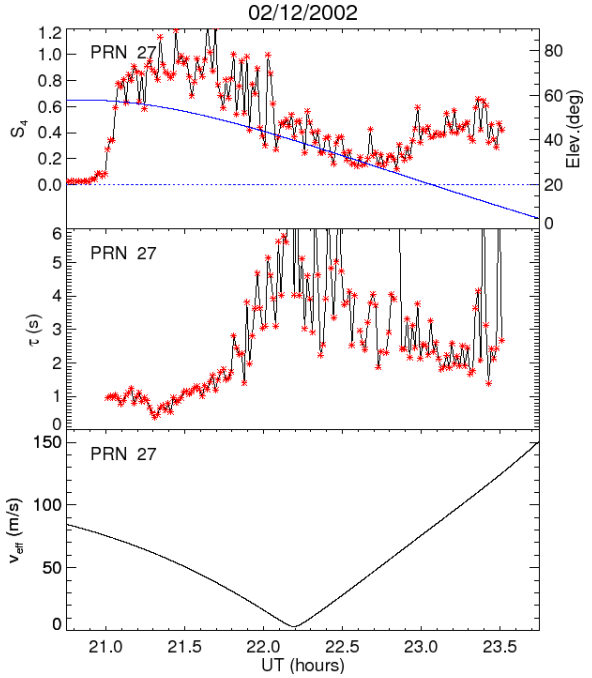

Fig. 9. Time variation of S_4 (top), τ_I (middle), and v_{eff} (bottom) for PRN27 on 12 Mar 2002. The satellite elevation is shown in blue.

As a more direct example of this effect, we compare the raw C/No and phase for PRN04 and PRN27 during two periods during for which the S_4 values (and also satellite elevation angles) are approximately equal. Figures 10, 11, 12, and 13 respectively show for PRN27 the C/No, PSD of intensity, detrended carrier phase, and PSD of detrended carrier phase. Similarly, Figures 14, 15, 16, and 17 respectively show for PRN04 the C/No, PSD of intensity, detrended carrier phase, and PSD of detrended carrier phase. The value of S_4 is 0.8 in both cases, corresponding to relatively strong scatter.

Notice the faster fading rate for PRN04 (Figure 14) as compared to PRN27 (Figure 10). This difference is reflected in the two decorrelation times (the shorter value of 0.32 sec for PRN04 versus the longer value of 0.91 sec for PRN27). The PSD of intensity is broader and the high frequency tail is steeper for PRN04 (Figure 15) than for PRN27 (Figure 11), which suggests more intense scattering of the signal in the former case. Comparing the detrended phases, we see both larger and faster phase variations for PRN04 (Figure 16) as compared to PRN27 (Figure 12). Note how the most rapid changes in phase are coincident with the deepest signal fades (compare, for example, the rapid phase change occurring at ~27 sec in Figure 11 with the deep signal fade also occurring at this time in Figure 10). When the rate of fading is higher, these rapid phase changes will be more frequent and this causes increased stress on the receiver's phase locked loop (PLL).

The magnitude of phase fluctuations (but not their rate) is characterized by the phase scintillation index (1.37 for PRN04 and 0.56 for PRN27). Considering the PSD of phase, the magnitude of the spectrum is larger for PRN04 (Figure 17) where $T=4.68\times10^{-2}$ as compared to PRN27 (Figure 15) where $T=5.21\times10^{-3}$. The faster effective velocity for PRN04 has in effect shifted the temporal fluctuations to higher frequencies. In this respect, the scattering environment and the stress on the receiver's tracking loops is more severe for PRN04 but that fact is not reflected at all by the S_4 index.

Finally, it should be noted that the receiver lost lock on PRN04 at the end of this 60 second period, but continued to maintain lock on PRN27. While this is only one particular example, we will show later that for a similar level of S_4 the probability of loss of lock is statistically higher when the decorrelation time is shorter.

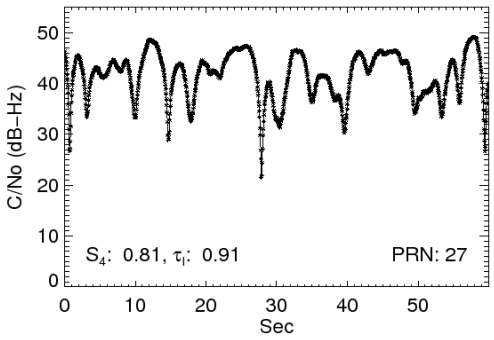

Fig. 10. C/No versus time for PRN27 starting at 21:10 UT on 12 Mar 2002. The satellite elevation angle is 57°.

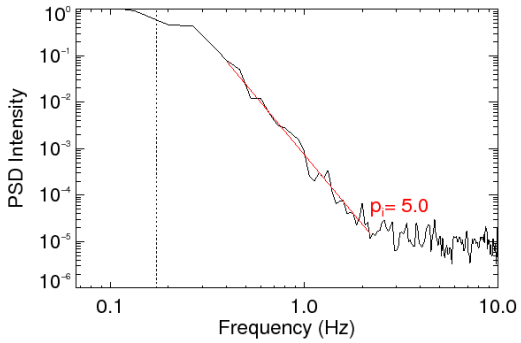

Fig. 11. Intensity PSD for PRN27 starting at 21:10 UT on 12 Mar 2002.

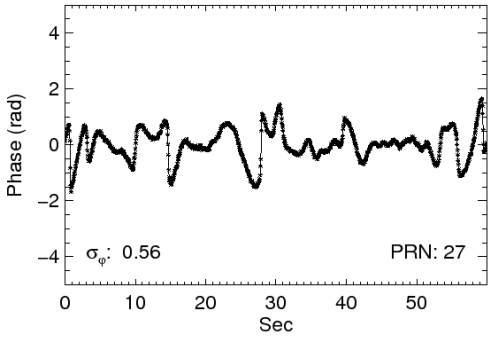

Fig. 12. Detrended carrier phase versus time for PRN27 starting at 21:10 UT on 12 Mar 2002.

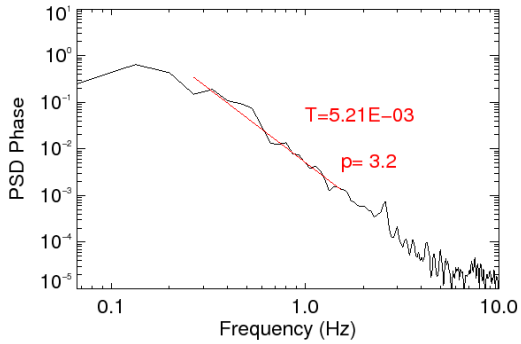

Fig. 13. Detrended phase PSD for PRN27 starting at 21:10 UT on 12 Mar 2002.

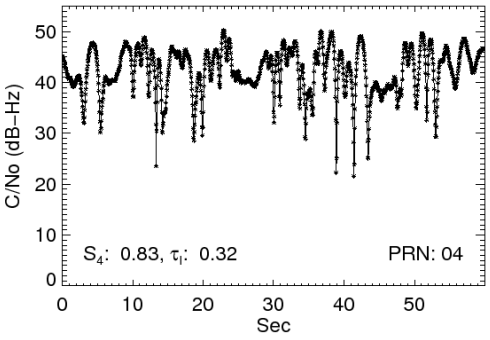

Fig. 14. C/No versus time for PRN04 starting at 22:18 UT on 12 Mar 2002. The satellite elevation angle is 55°.

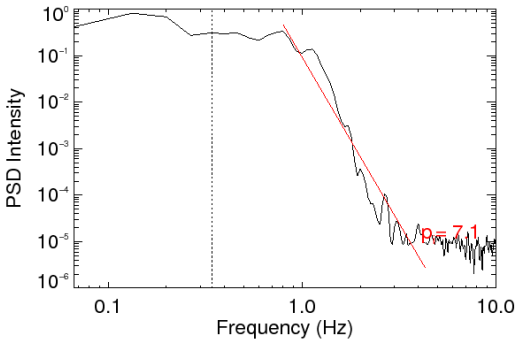

Fig. 15. Intensity PSD for PRN04 starting at 22:18 UT on 12 Mar 2002.

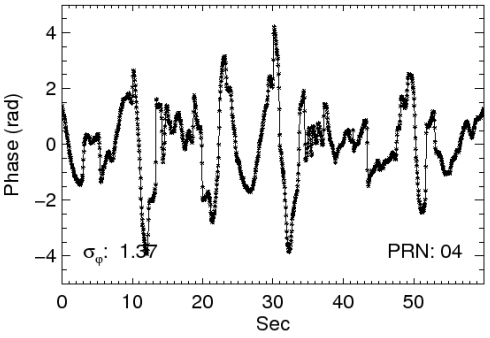

Fig. 16. Detrended carrier phase versus time for PRN04 starting at 22:18 UT on 12 Mar 2002.

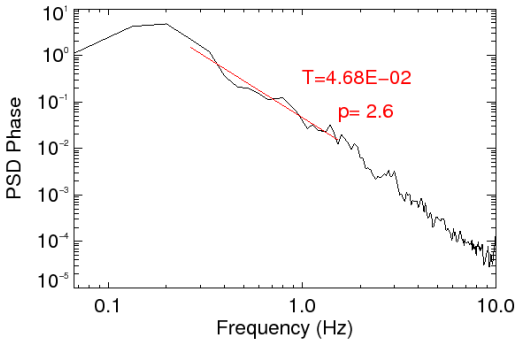

Fig. 17. Detrended phase PSD for PRN04 starting at 22:18 UT on 12 Mar 2002.

RELATIONSHIPS BETWEEN THE SCINTILLATION PARAMETERS

In this section we explore the relationships between the scintillation parameters and how they influence loss of lock occurrence. One of the most fundamental of the parameters is the phase spectral index, which is related to the spectral index of 3D electron density variations in the ionosphere. This relationship is more direct when the scatter is relatively weak. In strong scatter, the rapid phase transitions caused by diffraction tend to drive the phase spectral index to that for a discontinuous process, namely 2.0 [Rino et al., 1980]. Figure 18 shows a histogram of the phase spectral index for all samples with fluctuations well above the phase noise floor of the receiver. The value of 2.6 we observed is consistent with the observations made by other authors at Ascension Island. For example, Basu et al. [1987] measured the phase spectral index 2.4 by monitoring 244 MHz signals from a geostationary satellite.

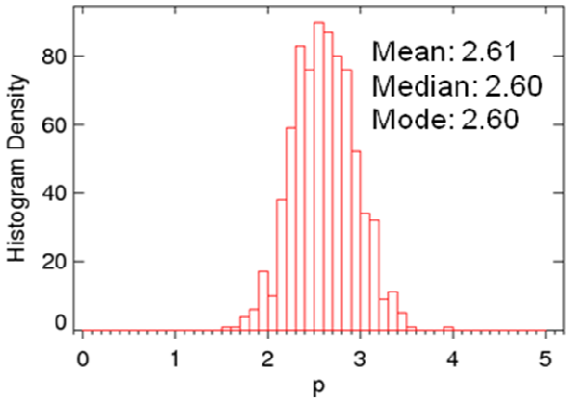

Fig. 18. Histogram of the phase spectral index over the campaign.

Figure 19 shows a scatter plot of S_4 versus τ_I. Note that for moderate to large values of τ_I, a wide range of S_4 values are observed. This indicates that the rate of fading and depth of fading are relatively independent, except when τ_I is short. When τ_I is very short, the value of S_4 approaches 1.0, which is indicative of saturation. As the scattering becomes more severe, the decorrelation time decreases with increasing perturbation strength, whereas the S_4 index saturates to a median value of 1.0 [Rino et al., 1980].

Like all of the scatter plots in this section, and also Figure 1, the points in Figure 19 are colored red if the receiver lost lock at the end of the 60 second interval over which the statistics were calculated, and green if there was no loss of lock for at least 4 additional minutes following this interval. One can see from this figure that most of the samples with short τ_I and large S_4 were accompanied by a loss of lock.

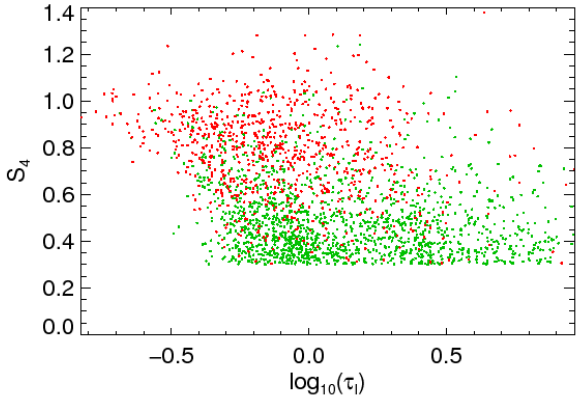

Fig. 19. Scatter plot of S_4 versus τ_I. Red dots indicate loss of lock, while green dots indicate unbroken (continuous) tracking.

Figure 18 shows a scatter plot of S_4 versus σ_φ. Both parameters tend to increase together, but as S_4 increases a wider range of σ_φ values is observed. In other words, a given level of amplitude fading can be associated with either small or large phase fluctuations being admitted by the phase detrend filter. This suggests that monitoring the value of S_4 alone may be insufficient to determine the level of stress on the receiver's PLL. We emphasize that only phase spectral content corresponding to frequencies larger than f_c=0.1 Hz contributes to the values of σ_φ reported here. For a similar propagation geometry, these values of the RMS phase fluctuations may be scaled to other cutoff frequencies (f_n) by multiplying the given values by $(0.1/f_n)^{(p-1)/2}$, where p~2.6 is the phase spectral index we observed [Rino et al., 1980, Basu et al., 1980].

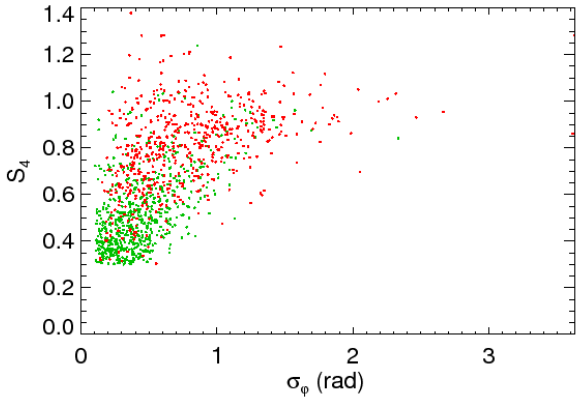

Fig. 20. Scatter plot of S_4 versus σ_φ.

Figure 21 shows a scatter plot of σ_φ versus τ_I. Two distinct regimes are visible in the plot. For values of τ_I less than about 1 second, σ_φ increases approximately linearly with decreasing values of $\log_{10}(\tau_I)$. For values of of τ_I longer than about 1 second, σ_φ approaches the phase noise floor of the receiver and may no longer accurately reflect ionospheric conditions.

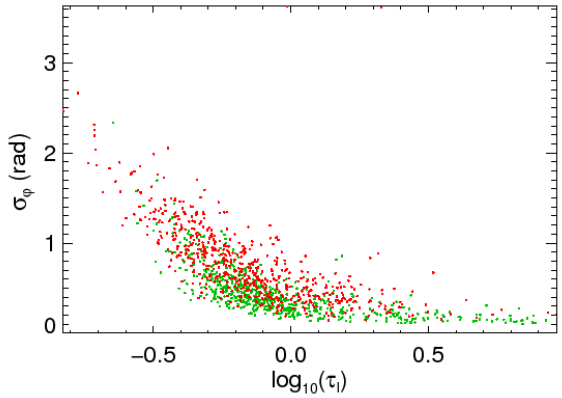

Fig. 21. Scatter plot of σ_φ versus τ_I.

In Figure 22, a plot of σ_φ versus T is shown. Because our detrend filter admits only phase spectral content corresponding to frequencies higher than our chosen cutoff, σ_φ is related to T according to $\sigma_\varphi^2=2T/[(p-1)f_c^{p-1}]$, assuming that a power law adequately describes the phase PSD and that diffraction effects on the phase can be neglected [Rino 1979]. Our observations follow this theoretical curve fairly closely, except for small values of σ_φ which may be corrupted by receiver noise, and for very large values of σ_φ for which we have a limited number of samples.

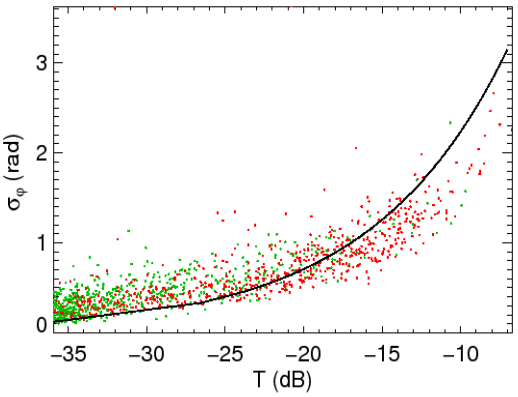

Fig. 22. Scatter plot of σ_φ versus T. Over plotted is the theoretical curve $\sigma_\varphi=[2T/((p-1)f_c^{p-1})]^{1/2}$.

In this paper we have emphasized the important role of the rate of fading, in addition to the depth of fading, in determining the impact on the performance of the GPS tracking loops. For this reason, it would be instructive to understand how the rate of fading is related to the scattering environment and the satellite motion. In the work of Rino [1980], later confirmed by other authors (e.g. Basu et al., 1987), it is shown that when the scattering is weak the intensity decorrelation time is a monotonic function of the Fresnel zone radius divided by the effective scan velocity. More precisely, there is a function f(y;ν) such that

$$\tau_I = Kf(Z^{1/2}/v_{eff};\nu) \tag{4}$$

where K is a constant and Z is the Fresnel zone parameter,

$$Z = \frac{\lambda z_R \sec\theta}{4\pi} \tag{5}$$

In the above, z_R is the reduced propagation distance which accounts for the spherical curvature of the wavefronts. It is given by

$$z_R = z_1 z_2 / (z_1 + z_2)\,, \tag{6}$$

where z_1 and z_2 are the vertical distances from the receiver and source to the ionospheric penetration point, respectively. Figure 23 shows a scatter plot of τ_I versus $Z^{1/2}/v_{eff}$ for those samples with $S_4<0.6$. The theoretical curve $\tau_I=Z^{1/2}/v_{eff}$ is also shown (where K=1 and f is the identity function), and appears to fit the observations quite well, although the spread increases substantially with τ_I. This spread may be due, in part, to difficulty in estimating long values of the decorrelation time using a fixed 60 second window to compute the statistics. We are interested primarily in fast rates of fading, however, since the stress on the GPS tracking loops is increased in this case. Equation (4), therefore, offers a useful way to predict the rate of fading based on the satellite motion which is known *a priori* (i.e. independently of the scattering), so long as the scattering is weak and the plasma drift velocity can be reasonably estimated.

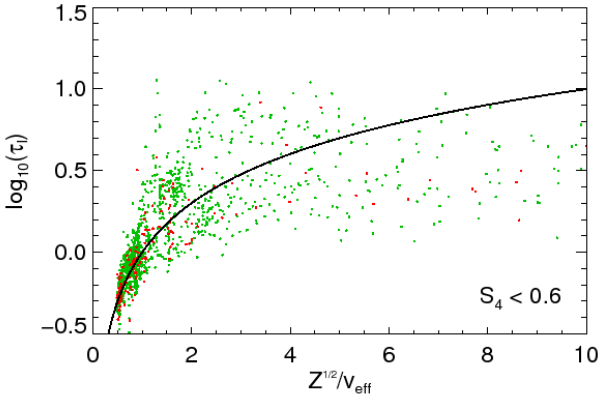

Fig. 23. Scatter plot of τ_I versus $Z^{1/2}/v_{eff}$ for samples with $S_4<0.6$. Over plotted is the theoretical curve $\tau_I=Z^{1/2}/v_{eff.}$

When the scattering is very strong, the intensity decorrelation time depends only on T and ν, provided $0.5<\nu<1.5$ [Rino, 1980]. Under these conditions, the autocorrelation function of intensity asymptotically approaches the square of the mutual coherence function, and τ_I may be expressed as:

$$\tau_I \sim T^{-1/(2\nu-1)}\left[\frac{4\pi^{2\nu-1/2}\Gamma(3/2-\nu)}{(2\nu-1)\Gamma(\nu)}C\right]^{-1/(2\nu-1)} \tag{7}$$

where C=-$\log_e(1/2)$. Figure 24 shows a scatter plot of τ_I versus T for those samples with S_4>0.9. As T increases, the decorrelation time converges to the theoretical result more closely, suggesting that we are indeed observing multiple scatter from a thick layer of ionospheric irregularities (strong saturation).

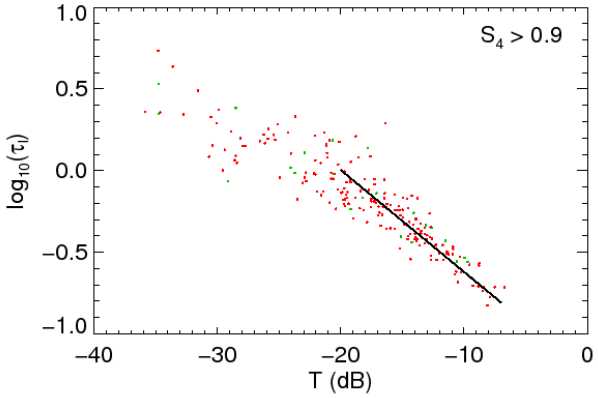

Fig. 24. Scatter plot of τ_I versus T for samples with S_4>0.9. Over plotted is the theoretical curve given in (7).

THE PROBABILITY OF LOSING LOCK

In this section we present quantitative statistics for the occurrence rate of the scintillation parameters and the probability of loss of lock as functions of these parameters. As in earlier sections, the data is divided into three categories: 1) samples for which a loss of lock occurred at the end of the 60 second observation window, 2) samples which are more than 4 minutes away from the next loss of lock event, and 3) all other samples. Samples which do not fall into either of the first two categories are excluded from the statistics since they may be ambiguous with regard to loss of lock. The probability of losing lock is computed by dividing the number of samples in category 1 by the number of samples in both categories 1 and 2 (i.e. all samples except the possibly ambiguous samples in category 3). If there are fewer than 8 samples any histogram bin, we do not compute a probability for that bin. Finally, we used a non-linear least squares technique to numerically fit the probability of losing lock with a function of following form:

$$P(x) = \frac{1}{2}\left[1 + \mathrm{Erf}\left(\frac{x - c_3}{c_4}\right)\right] \qquad (8)$$

where x represents the scintillation parameter under consideration, Erf(x) is the standard Error function, and c_3 and c_4 are coefficients to be determined. These coefficients are given in tables at the end of this section, and may be used to reproduce the empirical fits shown here for use in GPS modeling and simulation of GPS tracking performance and positioning accuracy (e.g. Carrano et al. [2005]).

For example, Figure 25 shows a histogram of the S_4 index. The blue shaded bars indicate the number of samples in category 1 (i.e. loss of lock), while the red bars indicate the number of samples in categories 1 and 2 (i.e. all samples except those in category 3 which may be ambiguous). Figure 26 shows the ratio of these two populations, which gives the probability of losing lock as a function of S_4. The function (8) has been fitted to these probabilities with x=S_4, and the coefficients of the least squares fit are given in Table 2, along with the chi values. Also shown are the values of S_4 which correspond to 50% and 90% probability of losing lock, which are 0.70 and 0.97, respectively. As expected, when S_4 is low very few loss of lock events are observed. As S_4 increases to the point to saturation, most samples are associated with a loss of lock.

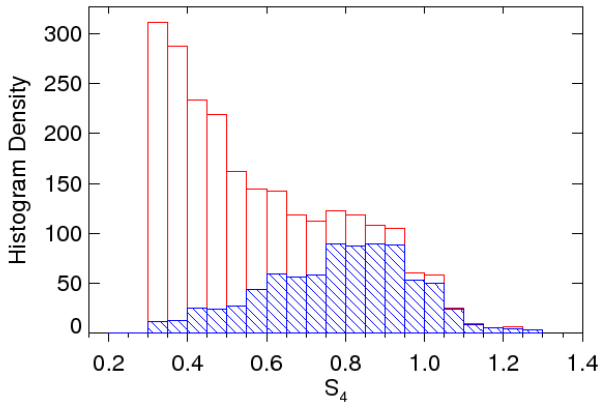

Fig. 25. Occurrences of S_4 that are associated with a loss of lock event (blue), and all samples (red).

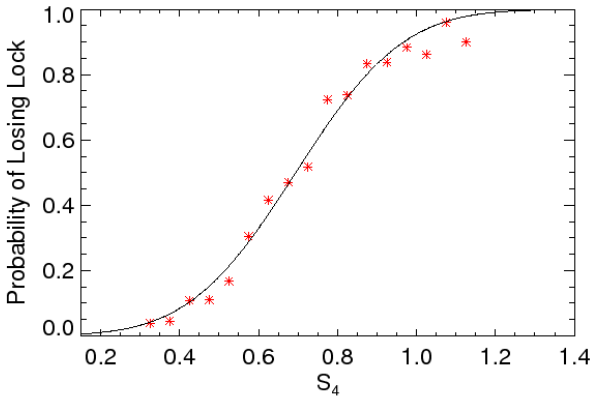

Fig. 26. Probability of losing lock versus S_4.

Figure 27 Shows a histogram of τ_I where, as before, the blue shaded bars show the number of samples in category 1 (i.e. loss of lock), while the red bars indicate the number of samples in both categories 1 and 2 (i.e. all samples except the possibly ambiguous ones in category 3). Figure 28 shows the ratio of these two populations, which gives the probability of losing lock. The function (8) is fitted to these probabilities using x=log10(τ_I) in this case, and the coefficients of the fit are given in Table 2. When the

decorrelation time is very long, very few loss of lock events are observed. As τ_I decreases, the number of loss of lock events increase.

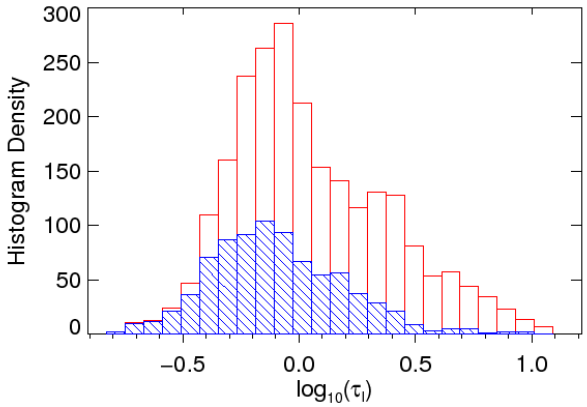

Fig. 27. Occurrences of τ_I that are associated with a loss of lock event (blue), and all samples (red).

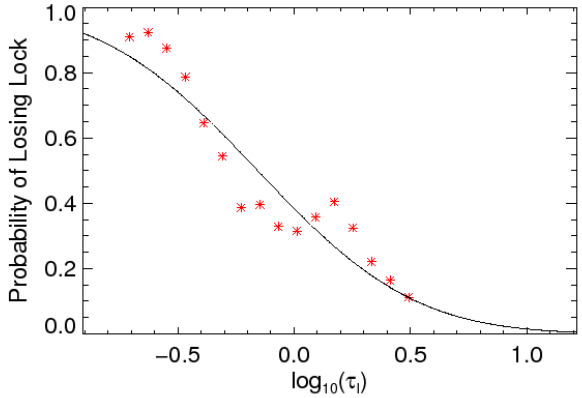

Fig. 28. Probability of losing lock versus τ_I.

Thus far, we have expressed the probability of losing lock as functions of S_4 and τ_I separately. Considering the probability of losing lock as function of τ_I alone is somewhat misleading, however, since the rate of fading should have minimal impact on loss of lock occurrence if the level of fading is low. Therefore, it is informative to consider the joint probability of losing lock, as a function of both S_4 and τ_I together.

Figure 29 shows a 2D histogram of S_4 and τ_I for all samples (categories 1 and 2, with ambiguous samples excluded). The configuration which occurred most frequently in the data was low S_4 with τ_I slightly less than 1. Figure 30 shows a 2D histogram of S_4 and τ_I for those samples associated with a loss of lock (category 1). The most frequent configuration in this case was S_4~0.8-0.9 and τ_I slightly less than 1. While we might have expected this distribution to peak at higher values of S_4, the number of samples with very large S_4 values was limited. Figure 31 shows the ratio of samples in Figures 30 and 29, which gives the probability of losing lock as a function of both S_4 and τ_I. If there are fewer than 5 samples any 2D histogram bin, we do not compute a probability for this bin. As expected, the probability of losing lock is highest when S_4 is large and τ_I is small. It is interesting to note that for each fixed level of S_4 the probability of losing lock generally increases as τ_I decreases (except, perhaps, for the very largest values of S_4, for which we may have insufficient samples for reliable statistics). This is consistent with our earlier observations.

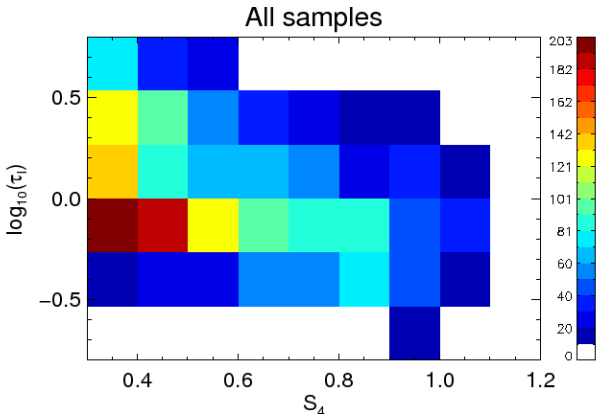

Fig. 29. Histogram of both S_4 and τ_I (all samples).

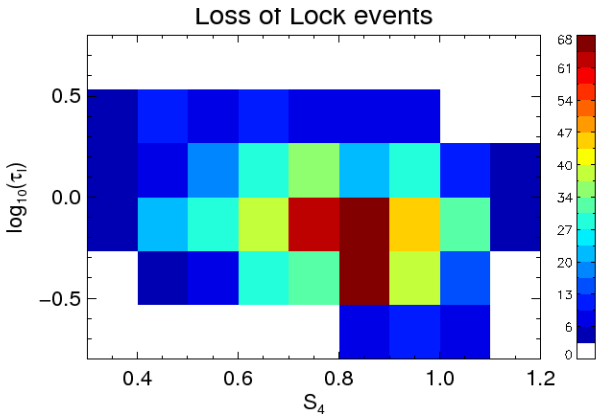

Fig. 30. Histogram of both S_4 and τ_I (loss of lock events).

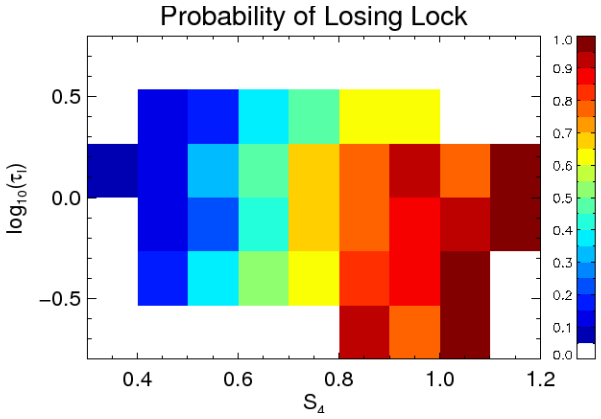

Fig. 31. Probability of losing lock versus both S_4 and τ_I.

To make this observation even more quantitative, we binned the observations into moderate ($0.3<S_4<0.6$),

strong ($0.6<S_4<0.9$), and very strong ($0.9<S_4<1.2$) scintillation conditions and then computed the probability of losing lock as a function of τ_I. The results are shown in Figure 32, and the parameters of the least-squares fit are given in Table 3. For moderate to strong scatter the probability of loss of lock increases as the decorrelation time decreases. This trend may not hold for the strongest scattering conditions, for which the probability of losing lock appears to be roughly independent of τ_I.

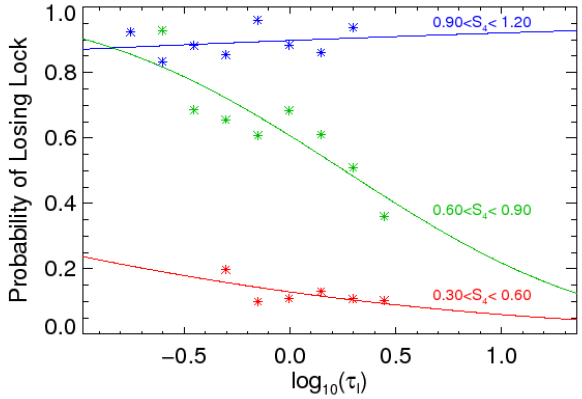

Fig. 32. Probability of losing lock versus τ_I for three different ranges of S_4 values.

Figure 33 shows a histogram of σ_φ. Low values of σ_φ were accompanied by infrequent loss of lock, whereas high values were usually associated with loss of lock. Figure 34 shows the probability of losing lock versus σ_φ. The parameters of the least squares fit are given in Table 2. The chances of losing lock are 50% when σ_φ is 0.60 radians and 90% when σ_φ is 1.36 radians. These values would change if a different detrend filter cutoff were used, but in that case one could scale the RMS phase fluctuations from the specific cutoff that was used to a cutoff of 0.1 Hz as described in the previous section to make use of this empirical fit.

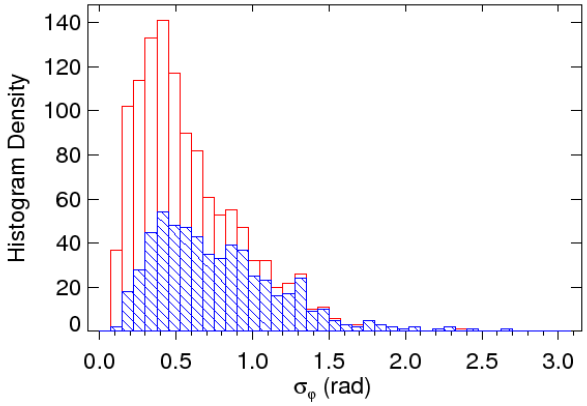

Fig. 33. Occurrences of σ_φ that are associated with a loss of lock event (blue), and all samples (red).

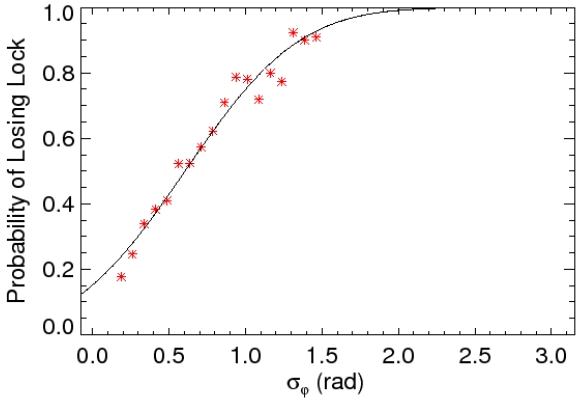

Fig. 34. Probability of losing lock versus σ_φ.

A histogram of the phase PSD value at a frequency of 1 Hz, expressed in dB, is shown in Figure 35. When T is small the chances of losing lock are small, and the chance increases with increasing T. Figure 36 shows the probability of losing lock as a function of T, and the parameters of the least squares fit are given in Table 2.

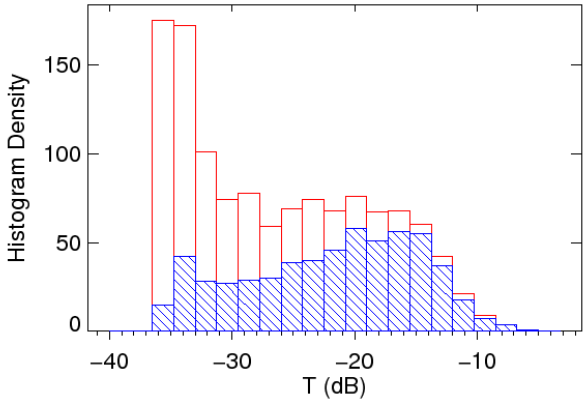

Fig. 35. Occurrences of T that are associated with a loss of lock event (blue), and all samples (red).

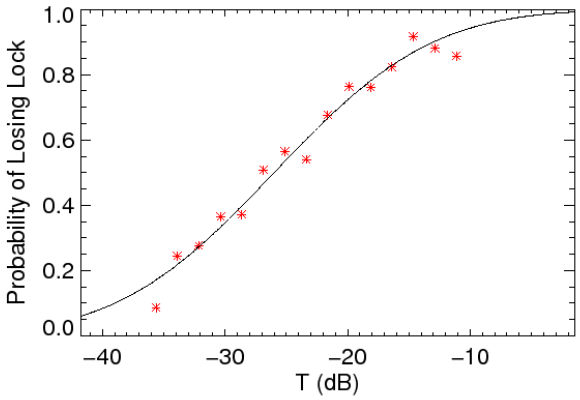

Fig. 36. Probability of losing lock versus T.

Equations (1), (2), and (3) enable one to compute the vertically integrated strength of turbulence at the 1 km scale (C_kL), given the parameter T and the propagation geometry. A histogram of C_kL is shown in Figure 37. The probability of losing lock as a function of C_kL is shown in Figure 38.

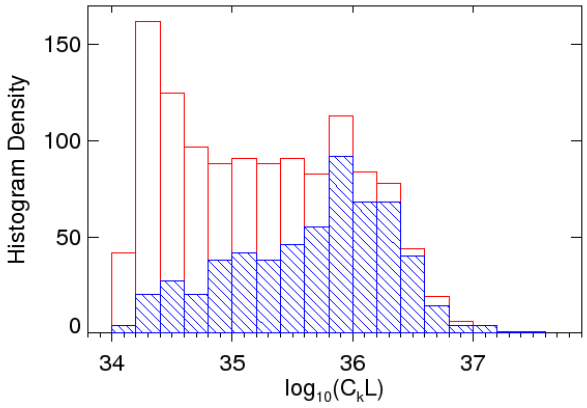

Fig. 37. Occurrences of C_kL that are associated with a loss of lock event (blue), and all samples (red).

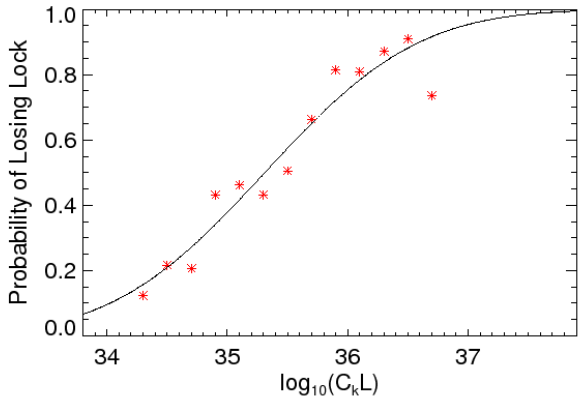

Fig. 38. Probability of losing lock versus C_kL.

Table 2. Coefficients of the nonlinear least-squares fit (equation 8) to the probability of losing lock as a function of the scintillation parameters. Also shown are the chi values and the values of the fitted functions sampled at 50% and 90% probability.

Quantity	**c_3**	**c_4**	**χ**	**50%**	**90%**
S_4	0.69	0.30	0.043	0.70	0.97
$\log_{10}(\tau_I)$	-0.16	-0.75	0.093	-0.16	-0.84
σ_φ (rad)	0.61	0.83	0.044	0.60	1.36
$\log_{10}(T)$	-2.61	1.48	0.043	-2.61	-1.27
T (dB)	-25.99	14.33	0.045	-25.97	-13.01
$\log_{10}(C_kL)$	35.31	1.42	0.079	35.31	36.60

Table 3. Coefficients of the nonlinear least-squares fit (equation 8) to the probability of losing lock as a function of the decorrelation time for specific values of S_4. Also shown are the chi values of the fit.

Quantity	**A**	**B**	**χ**
$\log_{10}(\tau_I)$, $0.3<S_4<0.6$	-2.67	-3.34	0.032
$\log_{10}(\tau_I)$, $0.6<S_4<0.9$	0.26	-1.35	0.084
$\log_{10}(\tau_I)$, $0.9<S_4<1.2$	-8.96	9.98	0.047

THE TIME TO REACQUIRE

In Figures 5 and 6 we showed a histogram of the time to reacquire the GPS signal in a stable manner after a loss of lock event. In this section we show that the longest times to reacquire were associated with short decorrelation times. This suggests that acquisition of the signal is more difficult when the signal is fluctuating rapidly, which is perhaps not surprising.

Figure 39 shows a scatter plot of τ_I versus the time to reacquire. Virtually all those samples for which the time to reacquire exceeds a few minutes correspond to a decorrelation time of less than one second. Note that the 95% occurrence of the time to reacquire was 4 minutes, so this observation applies only for the tail of the distribution. Those samples for which the time to reacquire was shorter than a few minutes showed no obvious dependence on the decorrelation time.

We have shown (Figure 23) that when the scattering is weak then τ_I varies like $Z^{1/2}/v_{eff}$. This parameter depends on the satellite motion and plasma drift, but not on the perturbation strength. Figure 40 shows a scatter plot of $Z^{1/2}/v_{eff}$ versus the time to reacquire. The similarity between Figures 40 and 41 suggest that we can anticipate when it will be particularly challenging to reacquire a satellite in the presence of scintillation based on the satellite motion and plasma drift without detailed knowledge of the scattering.

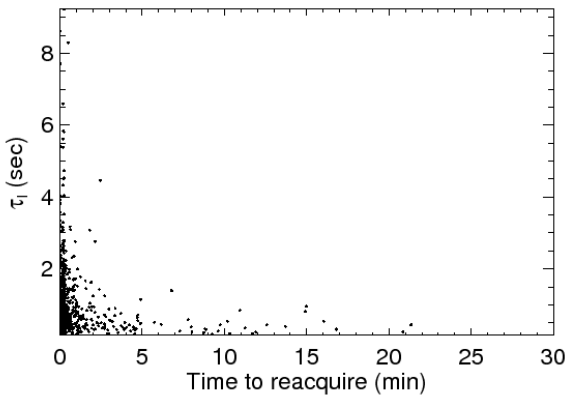

Fig. 39. τ_I versus the time to reacquire.

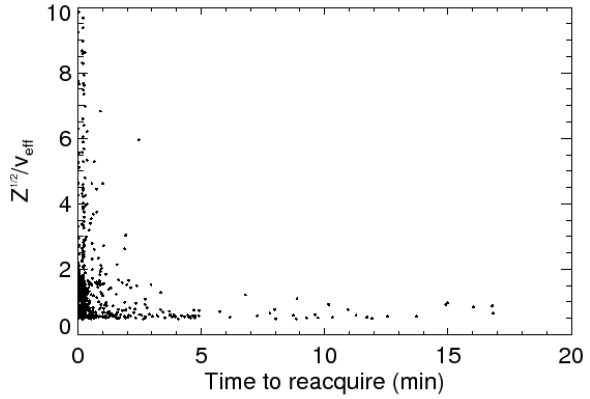

Fig. 40. $Z^{1/2}/v_{eff}$ versus time to reacquire.

CONCLUSIONS

We have analyzed a dataset collected with an Ashtech Z-XII survey grade GPS receiver at Ascension Island during the solar maximum year of 2002. This campaign exhibited some of the most disturbed ionospheric conditions under which high-rate GPS observations have to date been systematically analyzed. We have established that multiple scattering within an extended layer of irregularities was occurring (strong saturation), in that the decorrelation time of intensity approached the decorrelation time of the square of the mutual coherence function, as predicted by theory.

We demonstrated that the rate of fading, as quantified by the decorrelation time, is an important factor in causing loss of lock, in addition to the depth of fading. We presented cases where the S_4 index (and also the elevation angle) is the same for different satellites but the rate of fading is different, and showed that an increased number of loss of lock events and data gaps is associated with the higher fading rate. Since the fading rate is related to the effective scan velocity through the ionospheric irregularities, which is predictable *a priori*, we can anticipate which satellites the receiver is likely to lose lock on more frequently by virtue of the satellite's motion with respect to the magnetic field and plasma drift.

We computed histograms of the ionospheric statistics just prior to, and also away from, loss of lock occurrences. We computed the probability of losing lock from these observations, and provide least squares fits to the data for use in empirical models of GPS tracking and positioning accuracy. We determined that the 50% and 90% probability of losing lock for this receiver correspond to S_4 values of 0.70 and 0.97 respectively. Using a high-pass filter cutoff at 1 Hz, the 50% and 90% probability of losing lock corresponded to σ_φ values of 0.60 and 1.36 radians, respectively. These RMS phase values can be scaled for other detrend filter cutoff values using the approach described in the paper.

We found a relationship between extended reacquisition times and a geometry-dependent parameter that does not depend on the perturbation strength. This suggests the possibility of anticipating when a GPS receiver may have difficulty reacquiring a particular satellite based on geometrical considerations and without detailed knowledge of the scattering environment. While the probabilities of losing lock and reacquisition times we report may be specific to a particular GPS receiver model and tracking loop design, our observations that these quantities depend on the velocity of satellite motion with respect to the magnetic field and plasma drift is expected to be a general result (i.e. receiver independent).

ACKNOWLEDGMENTS

This work was sponsored by Air Force contract FA8718-09-C-0041.

REFERENCES

Basu, S., E. M. MacKenzie, Su. Basu, E. L. Costa, P. F. Fougere, H. C. Carlson, Jr., H. E. Whitney, *IEEE J. on Selected Areas in Communications*, v. sac-5, 2, Feb. 1987.

Carrano, C., K. Groves and J. Griffin, Empirical characterization and modeling of GPS positioning errors due to ionospheric scintillation, *Proc. of the Ionospheric Effects Symposium*, Alexandria, VA, May 3-5, 2005.

Kintner, P. M., B. M. Ledvina, and E. R. de Paula (2007), GPS and ionospheric scintillations, *Space Weather*, 5, S09003, doi:10.1029/2006SW000260.

Rino, C., E. Fremouw, The angle dependence of singly scattered wavefields, *J. Atmos. Terr. Phys.*, 39, 859-868, 1977.

Rino, C., A power law phase screen model for ionospheric scintillation, 1 Weak scatter, *Radio Sci*, 14, 1135-1145, 1979.

Rino, C. and J. Owen, The time structure of transionospheric radio wave scintillation, *Radio Sci*, Volume 15, Number 3, pp. 479-489, May-June 1980.

Seo, J., T. Walter, T-Y Chiou, P. Enge, Characteristics of deep GPS signal fading due to ionospheric scintillation for aviation receiver design, *Proc. of the Ionospheric Effects Symposium*, Alexandria, VA, May 2008.

Welch, P. D., The use of fast Fourier transform for the estimation of power spectra: a method based on time averaging over short, modified periodograms, *IEEE trans. on Audio and Electroacoustics*, vol. au-15, no. 2, 1967.